University of Groningen

Easy tuning of nanotexture and N doping of carbonaceous particles produced by spark discharge

Alfè, M.; Gargiulo, V.; de Luca, O.; Rudolf, P.; Zhang, B.; Sabia, P.; De Joannon, M.

IMPORTANT NOTE: You are advised to consult the publisher's version (publisher's PDF) if you wish to cite from it. Please check the document version below.

Document Version
Publisher's PDF, also known as Version of record

[Link to publication in University of Groningen/UMCG research database](#)

Contents lists available at ScienceDirect

Carbon Trends

journal homepage: www.elsevier.com/locate/cartre

Easy tuning of nanotexture and N doping of carbonaceous particles produced by spark discharge

M. Alfè [a,*], V. Gargiulo [a], O. de Luca [b], P. Rudolf [b], B. Zhang [c], P. Sabia [a], M. De Joannon [a]

[a] *Istituto di Scienze e Tecnologie per l'Energia e la Mobilità Sostenibili (CNR-STEMS), Via Guglielmo Marconi, 4, I 80125 Naples, Italy*
[b] *Zernike Institute for Advanced Materials, University of Groningen, Nijenborgh 4, NL-9747 AG Groningen, Netherlands*
[c] *Shenyang National Laboratory for Materials Science, Institute of Metal Research, Chinese Academy of Sciences, 72 Wenhua Road, Shenyang, 110016, China*

ARTICLE INFO

ABSTRACT

A better understanding of the effects of carbonaceous particulates in air pollution on human health and on the transmission of viruses requires studies with artificially produced aerosols that mimic the real ones. To produce such aerosols, methods to precisely tailor the morphology as well as the physical and chemical properties of carbon-based nanomaterials are crucial. Here we describe a facile and flexible approach to produce carbon-based nanoparticles with tailored N content by spark discharge utilizing graphite rods. Carbon-based nanoparticles with different nanotexture and N doping could be obtained by simply changing dilution gas (nitrogen, argon) and dilution gas purity (99 and 99.999%). The effect of the discharge frequency (50, 300 Hz) was also explored. The carbon-based nanoparticles were characterized by Fourier transform infrared and X-ray photoelectron spectroscopy, thermogravimetric analysis, and transmission electron microscopy. We find that the nanotexture is strictly linked to the chemical reactivity and to the surface chemistry. The use of N_2 as dilution gas allowed for the incorporation of significant amounts of nitrogen (5–7 wt.%) in the carbonaceous particle network mainly as pyrrolic N, graphitic N and N-oxide functional groups.

1. Introduction

Carbonaceous particulates from coal, fuel or wood combustion are harmful to human health and responsible for many chronic diseases, including cardiopulmonary and metabolic diseases, neurodegenerative conditions, cancer and low birthweight [1]. In addition, in the past years, several papers correlated atmospheric and meteorological scenarios to the outbreak of flu epidemics, like SARS and MERS [2,3]. Various studies undertaken since the start of the current COVID 19 outbreak point to the possibility that airborne particulate matter may be associated with an increased risk of SARS-CoV-2 transmission [4–6]. A high concentration of particulate matter has been suggested as possible co-factor in the transmission of the SARS-CoV-2, in order to explain the violent spread of the virus in highly industrialized and polluted areas [5–16].

This calls for more systematic investigations of the interactions between viruses and cells with particulate matter, which in turn require the easily reproducible generation of particles with pre-

dictable characteristics to mimic the airborne ones. An attractive tool for this purpose are Spark Discharge Generators (SDGs), where carbonaceous particles are produced through the vaporization of two graphite electrodes between which a tunable high voltage is applied. These particles, generated as aerosol, have been widely used in most studies involving human inhalation and exposure to mimic carbonaceous particles typically formed in combustion environment (flames, engines) [17]. A number of studies [18,19] also employ SDG-generated carbonaceous particles as soot model for diesel engine soot or carbon black because of their comparable mobility diameters and surface features and because SDGs offer the possibility to reproduce the differences between these two classes of particles by simply employing different discharge conditions.

The use of SDGs for the production of nanotextured particles is driven by several advantages of this technique, namely an easy operation, which allows for excellent control, reproducibility, and versatility of the type of particles generated, as well as the possibility to easily achieve reasonable yields using several SDGs in parallel [20]. By acting on the operative parameters (rod composition, spark discharge frequency, dilution gasses) [21,22] it is possible to incorporate different elements in the generated parti-

cles and to finely control the particle size distribution, and overall the chemical-physical features, including morphology at nanoscale level. An important feature of the carbonaceous nanoparticles generated by SDGs is their high surface purity [23], *i.e.* undesirable combustion byproducts as tar-like species or polycyclic aromatic hydrocarbons are absent.

A recent study by Hagen *et al.* (2020) showed that when spark discharge soot is produced using either argon or nitrogen as dilution gas, different amounts of N can be incorporated and not only the structure but also the reactivity can be modified. This is relevant both for the production of N-doped carbonaceous aerosols and for the use of such aerosols as model soot in specific experiments (soot reactivity, pressure drop and collection efficiency of particulate filters [22]). However, the influence of dilution gas purity has not been explored yet and a systematic analysis of the chemical functional groups introduced when using different dilution gasses is still missing.

This work closes this knowledge gap by investigating carbonaceous nanoparticles generated in a Palas GfG 1000 spark discharge system [19,24]. When operated with graphite electrodes, the carbon vapor generated in the arc discharge condenses into small primary particles, which then aggregate in clusters; these clusters can undergo further nucleation/condensation processes to form larger particles depending on the precise operation conditions. This work explores how the N incorporation as well as the surface functional groups and the chemical reactivity of carbonaceous particles produced from graphite rods in this type of discharge system can be tailored by acting on three parameters: dilution gasses (nitrogen, argon), dilution gasses purity and discharge frequency (50, 300 Hz). The chemical reactivity and the surface chemistry of the particles were evaluated by thermogravimetric analysis (TGA), X-ray photoelectron spectroscopy (XPS) and Fourier transform infrared spectroscopy (FTIR). Results concerning the elemental composition of the particles as well as the type and quantity of chemical bonds present, were correlated with the SDG operating parameters, and these findings were linked to the corresponding morphology and internal structural characteristics inferred from transmission electron microscopy (HRTEM) images.

2. Materials and methods

All the chemicals (ACS grade) used in this study were purchased from Merck - Life Science Srl (Milan, Italy).

2.1. Particles production

In the aerosol generator (GfG 1000, Palas GmbH, Karlsruhe), two 6 mm diameter graphite rod electrodes (purity 99.999%) were mounted at a distance of about 2 mm from one another and an argon shielding stream (3.5 L/min carrier gas flow, purity 99.999%) was fed through a narrow slit into the space between the electrodes to prevent oxidation of the carbon at high temperature and to act as carrier gas for removing all primary particles and ions between the electrodes before the next spark [22].

At the chamber exit, the aerosol was diluted in a concentric annular nozzle by nitrogen or argon delivered at a flow rate of 30 L/min. Gasses of minimum purity 99 and 99.999% were employed. The nominal amount of O_2 was 3 ppm in the case of low purity gasses and lower in the case of high purity gasses. The spark discharge frequency was set to 50 or to 300 Hz and the carrier gas flow rate (high purity Ar in all cases) to 3.5 L/min. In total eight different samples were produced *via* the spark generator, four with Ar and four with N_2 as dilution gas and for both gasses, both purities were tested with both spark frequencies; the corresponding sample names are reported in Table 1. The samples were collected on a polytetrafluoroethylene (PTFE) filter (Fluoropore, Milli-

Table 1
Sample production conditions and labeling.

Sample	Dilution gas	Gas purity	Spark frequency, Hz
P-hpAr-50	Ar	High	50
P-hpAr-300	Ar	High	300
P-lpAr-50	Ar	Low	50
P-lpAr-300	Ar	Low	300
P-hpN$_2$-50	N$_2$	High	50
P-hpN$_2$-300	N$_2$	High	300
P-lpN$_2$-50	N$_2$	Low	50
P-lpN$_2$-300	N$_2$	Low	300

pore, 0.45 μm porosity) located downstream of the generator, during a sampling time of 30 min each, and analyzed off-line.

2.2. Characterization methods

The elemental composition of the materials was estimated by a CHN 628 LECO elemental analyzer and using ethylene diamine tetraacetic acid (EDTA) as standard. The C, H, N contents were expressed as atomic percentage; the O content was evaluated by difference. Each measurement was repeated three times.

TGA was conducted in oxidative environment (air) on a Perkin–Elmer STA6000 thermogravimetric analyzer (gas flux 40 mL/min) from 50 °C up to 800 °C at a heating rate of 10 °C/min. Samples of approximately 5 mg were loaded in an alumina crucible thermally pre-conditioned up to 950 °C for an accurate evaluation of the mass losses.

FTIR spectra in the 450–4000 cm^{-1} range were recorded on a Perkin-Elmer Frontier MIR spectrophotometer in transmittance mode. The spectra were acquired on KBr pellets (1 wt.%); each spectrum was the sum of 8 scans and the resolution was set to 1 cm^{-1}.

Transmission electron microscopy (TEM) and high-resolution TEM (HRTEM) imaging was performed on a FEI Tecnai G2 F20 transmission electron microscope equipped with a field-emission gun which was operated at 200 kV. A Gatan camera (BM-UltraScan) was used to acquire the TEM images and the samples were observed at magnifications ranging from 2×10^5 to 1×10^6. The preparation of the samples was the following: the powders were dispersed in ethanol, then a droplet of this suspension was deposited onto a 200 mesh lacey carbon on Cu grid TEM sample holder and allowed to dry at room temperature.

XPS spectra were collected using a Surface Science SSX-100 ESCA instrument with a mono-chromatic Al K$_\alpha$ X-ray source (hν = 1486.6 eV). The samples were dispersed in chloroform and a small drop of the suspension was left to dry in air on a 150 nm thick gold film supported on mica (prepared as detailed in [25]). The pressure in the measurement chamber was maintained below 1×10^{-9} mbar; the electron take-off angle with respect to the surface normal was 37° and the analyzed spot had a diameter of 1000 μm. The energy resolution was set to 1.26 eV for both the survey spectra and the detailed spectra of the C1s, N1s, and O1s core level regions. Binding energies are referenced to the C1s peak centered at a binding energy of 284.8 eV [26]. All XPS spectra were analyzed using the least-squares curve-fitting program Winspec (developed in the LISE laboratory of the University of Namur, Belgium). Deconvolution of the spectra included a Shirley [27] baseline subtraction and fitting with a minimum number of peaks consistent with the chemical structure of the sample, considering the experimental resolution. The profile of the peaks was taken as a convolution of Gaussian and Lorentzian functions; peak positions are reported ±0.1 eV when deduced from a fit. The uncertainty in the peak intensity determination is 2% for the C1s and O1s core level regions, 4% for the N1s core level region.
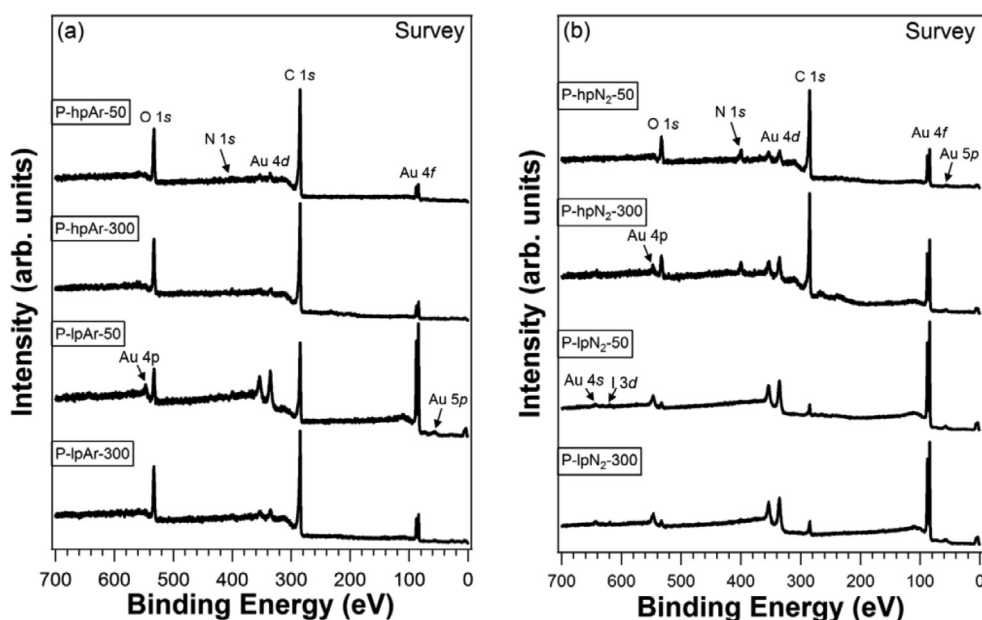
Fig. 1. Survey scan of carbon nanoparticles produced with high and low purity Ar (panel (a)) or with high and low purity N$_2$ (panel (b)) as dilution gas and two different spark frequencies.

Table 2
Chemical composition of the carbonaceous nanostructures estimated from elemental analysis (EA) and from X-ray photoelectron spectroscopy (XPS).

Sample	C, at.%(EA)	H, at.%(EA)	O, at.%(EA)	N, at.%(EA)	C, at.%(XPS)	O, at.%(XPS)	N, at.%(XPS)
P-hpAr-50	70.2	15.2	13.9	0.6	80.1	18.4	1.5
P-hpAr-300	70.2	13.4	14.4	2.0	81.6	16.7	1.7
P-lpAr-50	83.0	0	13.3	3.7	79.0	17.3	3.7
P-lpAr-300	79.1	3.7	16.6	0.6	80.8	17.7	1.5
P-hpN$_2$–50	78.1	5.9	10.1	5.8	82.1	10.8	7.2
P-hpN$_2$–300	77.6	10.1	6.2	6.1	85.3	9.3	5.4
P-lpN$_2$–50	72.9	14.1	8.2	4.7	79.6	16.0	4.4
P-lpN$_2$–300	80.5	3.6	10.8	5.0	78.7	15.5	5.8

3. Results and discussion

XPS spectroscopy provides insight on the elemental composition of the carbon nanostructures as well as on the chemical environment of the elements detected, while FTIR spectroscopy informs on the type of chemical bonds present. XPS survey scans of the nanoparticles produced with Ar and N$_2$ are shown in Fig. 1. All the expected elements are observed; C and O are the main constituents of the nanostructures produced with Ar as dilution gas, while a significant presence of N is observed when the dilution gas was N$_2$. The Au signature is ascribed to the gold surface where the samples were deposited, while the traces of iodine detected for two samples prepared using N$_2$ as dilution gas can be attributed to contamination in the low purity N$_2$.

Since X-ray photoelectron spectroscopy probes the near surface region, while elemental analysis (EA) gives information on the whole sample, in Table 2 the results of both techniques are compared. Note that XPS cannot detect hydrogen but is a quantitative technique, i.e. the atomic percentage of all elements present can be deduced from the intensity of the respective photoemission lines. A good general agreement is found between EA and XPS results. The particles produced with Ar as dilution gas present a quite constant O and N incorporation and no significant dependence on dilution gas purity is detected. The particles produced with N$_2$ as dilution gas present a higher N content up to 7 wt.%. The higher N content observed in this case agrees with the integration of more N into the carbon network, as observed in plasma processes carried out in pure nitrogen [28]. The N content resulted

slightly lower when low purity N$_2$ instead of high purity N$_2$ was used as dilution gas. This could be due to the competing incorporation of O, as confirmed by the fact that this element presents an inverse trend compared to N, namely more O incorporation occurs when low purity N$_2$ is used and less when high purity N$_2$ is employed.

The chemical environment of carbon, oxygen and nitrogen was evaluated by deconvoluting the C1s, O1s and N1s XPS spectra shown in Figs. 2 and 3 and summarized in Table 3, where the results of the fits in terms of binding energies (B.E.s), attribution of the various components to the type of bond, and relative contribution to the total spectral intensity are reported.

The C1s spectra of all samples (Figs. 2(a) and 3(a)) require six components to obtain a good fit; the main component at a B.E. of 284.8 eV (marked in blue in Figs. 2(a) and 3(a)) can be ascribed to C−C/C = C species, while the other peaks located at about 285.9 eV, 287.0 and 288.2 eV and 289.5 eV can be assigned to C−O/C−N (red), C−O-C (green), C = O (yellow), COOH (pink) bonds, respectively [29–32]. Moreover, the shake-up satellite (light green) at about 291.1 eV is typical for the presence of aromatic carbon.

The spectra of the O1s core level region of all samples are presented in Figs. 2(b) and 3(b), and contain three contributions; the peak at a B.E. of about 532.0 eV derives from C = O species (marked in yellow in Figs. 2(b) and 3(b)), while the components centered at about 533.2 eV and 534.6 eV correspond to C−O bond (red) and adsorbed water (light blue), respectively [33].

The presence of N and the type of bonds in which it is involved is determined by the N1s photoemission lines. The N1s
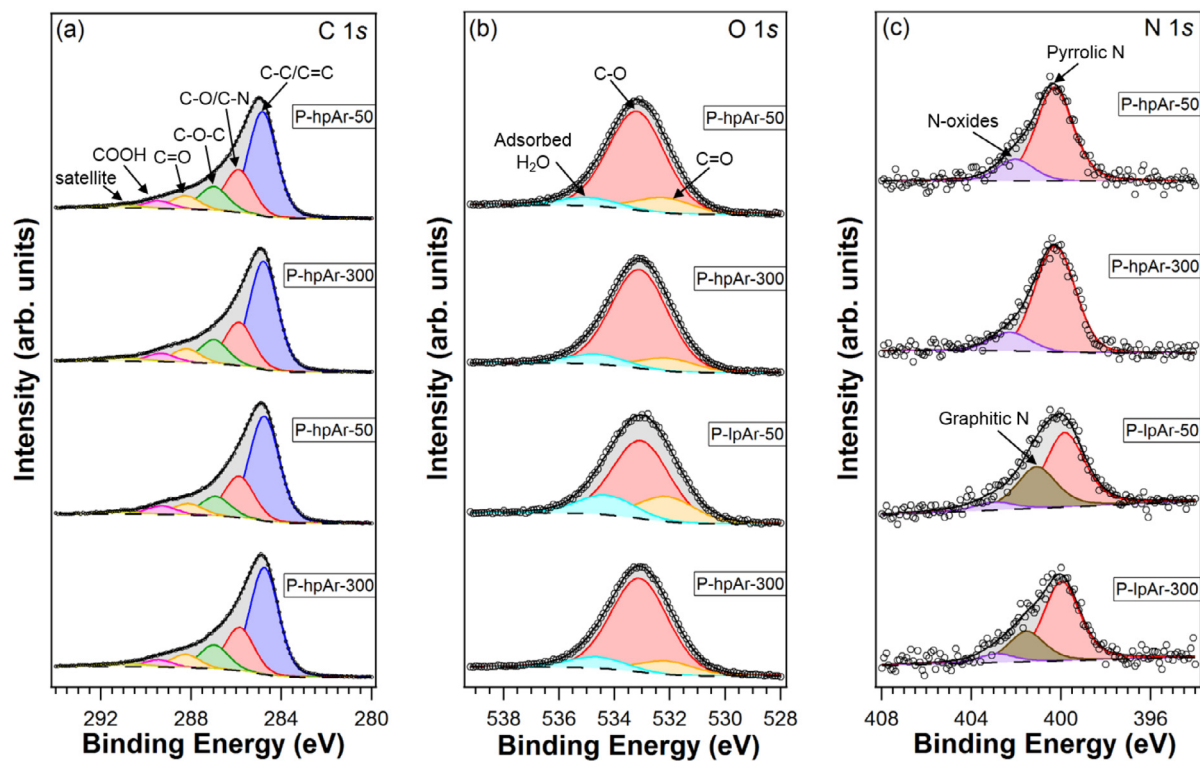
Fig. 2. XPS spectra of the C1*s* (a), O1*s* (b) and N1*s* (c) core level regions of carbon nanoparticles produced with high and low purity Ar as dilution gas and two different spark frequencies and corresponding fits (full lines); for the differently colored peaks see text.

Fig. 3. XPS spectra of the C1*s* (a), O1*s* (b) and N1*s* (c) core level regions of carbon nanoparticles produced with high and low purity N$_2$ as dilution gas and two different spark frequencies and corresponding fits (full lines); for the differently colored peaks see text.
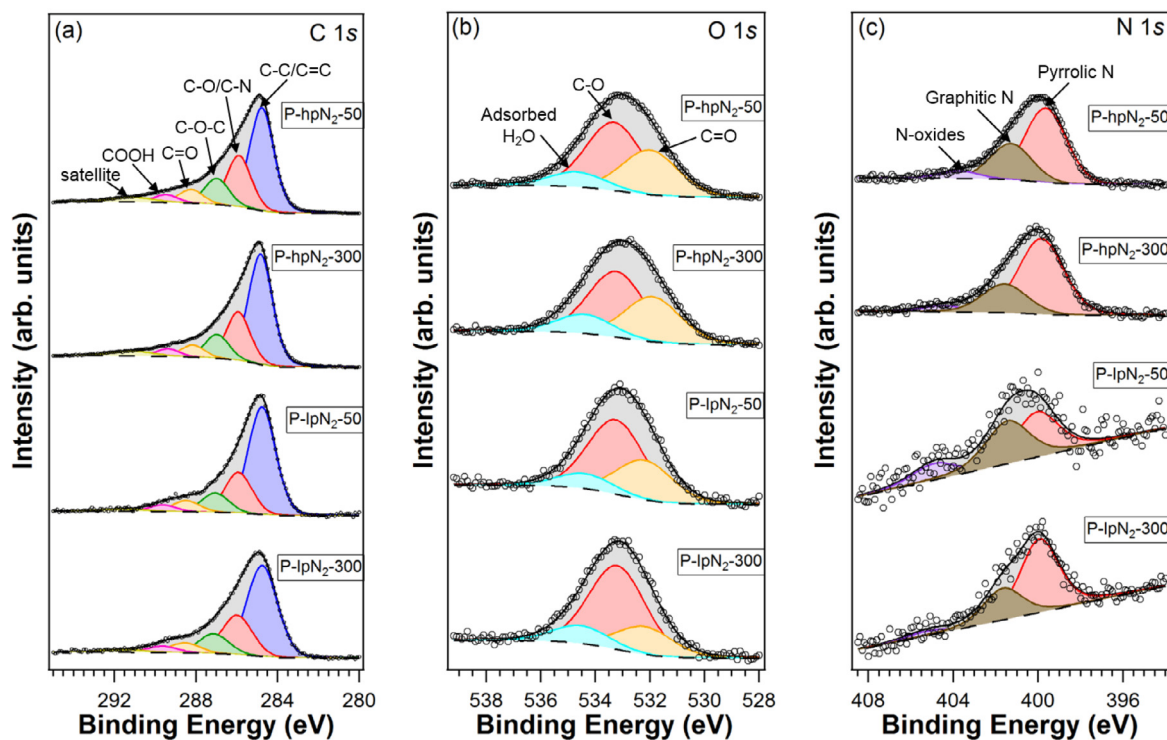
Table 3

Binding energies and percentages indicating how much the component contributes to the total C1*s*, N1*s* and O1*s* intensity; these percentages indicate the relative amounts of C, N, O atoms involved in each type of bond as deduced from the XPS measurements.

	Bond type	B.E. (eV)	FWHM (eV)	P-hpAr-50 %	P-hpAr-300 %	P-lpAr-50 %	P-lpAr-300 %	P-hpN$_2$–50 %	P-hpN$_2$–300 %	P-lpN$_2$–50 %	P-lpN$_2$–300 %
C1*s*	C–C/C = C	284.8	1.4–1.5	52.9	53.1	55.4	53.3	48.9	52.1	56.8	53.2
	C–OH/C–N	285.9	1.4–1.5	21.8	21.4	22.0	21.7	24.4	23.0	21.4	23.1
	C–O–C	286.9–287.1	1.4–1.5	12.2	11.9	10.4	12.0	12.4	11.3	10.2	11.5
	C = O	288.1–288.6	1.4–1.5	6.9	6.7	6.1	6.7	6.5	5.7	6.0	6.0
	COOH	289.5–289.6	1.4–1.5	4.0	4.2	4.6	3.7	3.8	3.7	3.5	3.8
	satellite	291.0–291.6	2.5	2.2	2.7	1.5	2.6	4.0	4.2	2.1	2.4
N1*s*	pyrrolic	399.7–400.3	1.9–2.3	80.8	85.0	59.9	66.8	63.0	68.4	43.1	66.7
	graphitic	401.1–401.6	1.9–2.3	–	–	33.5	25.7	30.8	26.0	41.1	29.0
	N-oxides	402.0–405.3	1.9–2.3	19.2	15.0	6.6	7.5	6.2	5.6	15.8	4.3
O1*s*	C = O	531.9 –532.2	2.4	12.5	16.2	20.4	11.4	35.0	34.7	30.8	21.5
	C-OH	533.1–533.3	2.4	80.6	76.9	63.6	79.0	53.3	50.6	57.6	64.8
	Adsorbed H$_2$O	534.3–535.0	2.4	7.0	6.9	16.0	9.6	11.7	14.7	11.6	13.7

spectra were deconvoluted into two or three contributions and the types of N-containing functionalities are reported in Table 3. The XPS spectra indicate the presence of pyrrolic N (marked in red in Figs. 2(c) and 3(c)), where one N atom is connected with two C atoms and one H atom in a five-membered ring; N-oxide functional groups (purple) as well as two types of graphitic N (brown), namely N atoms located either in the middle of a graphene segment or at graphite zigzag edges or vacancy sites [34–36]. It is also evident in Figs. 2 and 3 that when lower purity Ar or N$_2$ are used as dilution gas, (samples P-lpAr-50, P-lpAr-300, P-hpN$_2$–50, P-hpN$_2$–300, P-lpN$_2$–50, P-lpN$_2$–300) more N is incorporated into the graphitic network (graphitic N) rather than as peripheral N (pyrrolic-type N). When higher purity Ar is employed as dilution gas (samples P-hpAr-50 and P-hpAr-300) we still observe the presence of N (whose source comes supposedly from the gas impurities, N$_2$ < 5 ppm in the case of high purity Ar) but only in the form of N-oxide and pyrrolic N.

The FTIR spectra are reported in Fig. 4; the spectra are baseline-corrected, height-normalized and shifted for clarity.

All eight samples absorb very similarly and their infrared signals are mostly located in three regions: i) between 3100 and 3600 cm^{-1}, where broad bands due to exchangeable protons from N- and O-containing functional groups and adsorbed water are observed; ii) between 2800 and 3100 cm^{-1}, where one sees low-intensity signals ascribable to the stretching vibrations of aromatic and aliphatic C − H groups, probably arising from impurities in the graphite rods and in the argon carrier gas as already observed in [37–39]; iii) between 1750 and 1000 cm^{-1}, where signals ascribable to the stretching and bending vibrations of different O and N-containing functional groups and of adsorbed water overlap.

In all the cases the region below 1800 cm^{-1} is the richer in signals and the two types of samples show significant differences. In Fig. 5 an enlarged view of the FTIR spectra in the region between 2300 and 900 cm^{-1} is reported, contrasting particles generated with either Ar or N$_2$ in comparable conditions to better evidence differences and similarities. In the case of particles generated with Ar, the main absorption band at 1650 cm^{-1} is ascribed to the stretching of C = C in an aromatic network, the shoulder at 1720 cm^{-1} stems from the stretching of C = O in carbonyl and carboxylic groups, while the peaks at 1450, 1395, 1280, 1120 and 1075 cm^{-1} are associated mainly with stretching and bending modes of different C−O containing groups [40–46].

In the case of the particles produced with N$_2$, bands associated with the presence of N can clearly be observed. The signal at 2200 cm^{-1} is ascribable to the C−N triple bond stretching [46], the main band around 1600 cm^{-1} is assigned to overlapping signals from C = C and C = N stretching vibrations [44,46], while the shoulder at 1710 cm^{-1} is associated with the stretching of C = O bonds. The signals at 1455, 1390, 1365, 1280, 1125, and 1075 cm^{-1} de-
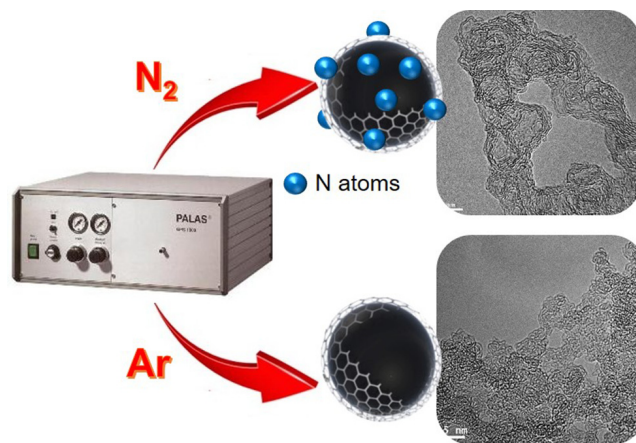

Fig. 4. FTIR spectra of carbon nanoparticles produced with high and low purity Ar (top panel) or with high and low purity N$_2$ (bottom panel) as dilution gas and two different spark frequencies.

rive mainly from stretching and bending modes of different C−O containing groups [40–46], suggesting the presence of the same oxygen containing groups present on the surface of the particles produced with Ar. Moreover, a band at 1210 cm^{-1} associated with the stretching mode of C−N bonds [47] is present, and this band is most intense for the particles produced with the lower spark discharge frequency and the higher purity of the dilution gas (Fig. 5).

As expected, the intensities of the bands around 1600 cm^{-1} and at 1210 cm^{-1} associated with N-containing groups are higher in the case of particles produced using N$_2$ as dilution gas. The intensities of these bands as well as of that related to C = O stretching are also influenced by the spark frequency and the gas purity. In particular, in the case of the particles produced with N$_2$ and a spark discharge frequency of 300 Hz, namely P-lpN$_2$–300 and P-hpN$_2$–300 (Fig. 5, panels (c) and (d)), no significant influence of
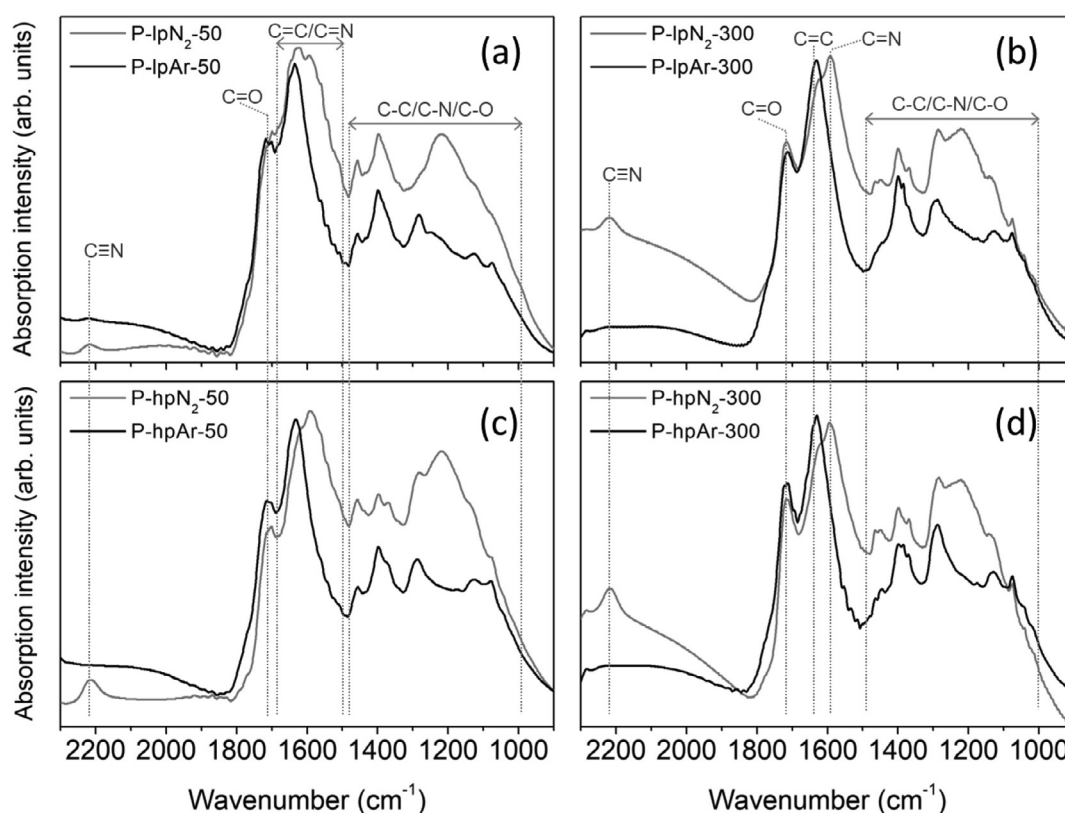
Fig. 5. Enlarged view of the 900–2300 cm^{-1} region of the FTIR spectra of carbon nanoparticles produced with low (panels (a) and(b)) and high purity (panels (c) and (d)) dilution gas and two different spark frequencies (50 Hz left panels, 300 Hz right panels).

the gas purity is observed, while in the case of particles produced at a spark discharge frequency of 50 Hz, namely P-lpN$_2$–50 and P-hpN$_2$–50 (Fig. 5, panels (a) and (b)), the two main bands associated to N-containing groups exhibit a lower intensity and the band associated to C = O appears as a small shoulder of the main peak at around 1600 cm^{-1}. In the case of nanoparticles produced with Ar, interestingly, the influence of the gas purity and the spark discharge frequency appears to be negligible.

The HRTEM images reported in Figs. 6 and 7 revealed a clear relation between the nature of the dilution gas and the size, structure and way of aggregation of the particles. In all of the cases, the micrographs evidenced an overall structural inhomogeneity, although primary particles are sometimes clearly distinguishable. The arrangement of the nanostructures does not seem to depend on spark discharge frequency with which the particles were generated.

In the case of particles produced with Ar as dilution gas, (Fig. 6), small and quite widely distributed, well-defined primary particles with average diameter ranging from 2 to 5 nm (Fig. 6, lower panels, circled) are discernible. These particle sizes are considerably smaller than that of soot typically produced in flames and engine environments [48–52]. Also the particle structure is very different from the typical chain-like structure of combustion products [48] and shows instead an overall fulleroid shape consisting of short and bent graphenic segments. Closed shells arising from fullerenes are clearly visible on the particles' surface (Fig. 6, lower panels, indicated by arrows). The observed structures are typical of GfG soot [17-19, 53], characterized by a non-negligible oxygen content.

The nanoparticles produced with N$_2$ as dilution gas have a completely different structure as seen in the micrographs of Fig. 7: the surface is smoother, the particles have more extended graphene sheets. In such nanoparticles, distinctive multi-layer features attributable to carbon onions [54] clearly emerge. These structures can be described as spherical or polyhedral, defective and disordered multiple shells with a hollow core extending up to 10 nm.

The higher curvature of these nanoparticles is driven by the dominant presence of pyrrolic N as observed in XPS, which results in five-membered rings in the graphenic arrangement. It is worth noting that such distinctive features appear to a lower extent when the low purity dilution gas is used for producing the P-lpN$_2$–300 particles.

The TGA profiles of all the carbon nanoparticles produced with both Ar and N$_2$ as dilution gas (Fig. 8) exhibit a continuous weight loss with a complete burn off before 750 °C.

For the most of the particles produced with Ar, the weight loss starts after 200 °C; only the particles produced at low spark frequency and with low purity gas begin to lose weight already below 200 °C, pointing out a higher structural inhomogeneity. The derivative thermogravimetric (DTG) curves reported in Fig. 8 show for all the particles produced with Ar (bottom right panel) a first event in the range 300–450 °C and a second important event peaked at 550 °C. This thermal behavior is in accordance with that reported for GfG soot produced with Ar as carrier gas [22,53]. Based on the discussion of the TEM images above, we suggest that this first loss at about 400 °C corresponds to the combustion of defect-rich primary particles [17]. The second weight drop at 600 °C can instead be assigned to the combustion of large primary particles or agglomerates with less defective/functionalized surfaces and, eventually, also of surface-bonded fullerenes produced in the spark-discharge of graphite [53]. Overall, the thermal behavior of the particles produced with Ar is only slightly influenced by the gas purity and the spark discharge frequency.

Conversely, the particles produced with N$_2$ exhibit a quite different thermal behavior, which is clearly influenced by the gas purity and the spark discharge frequency. Their DTG curves are char-
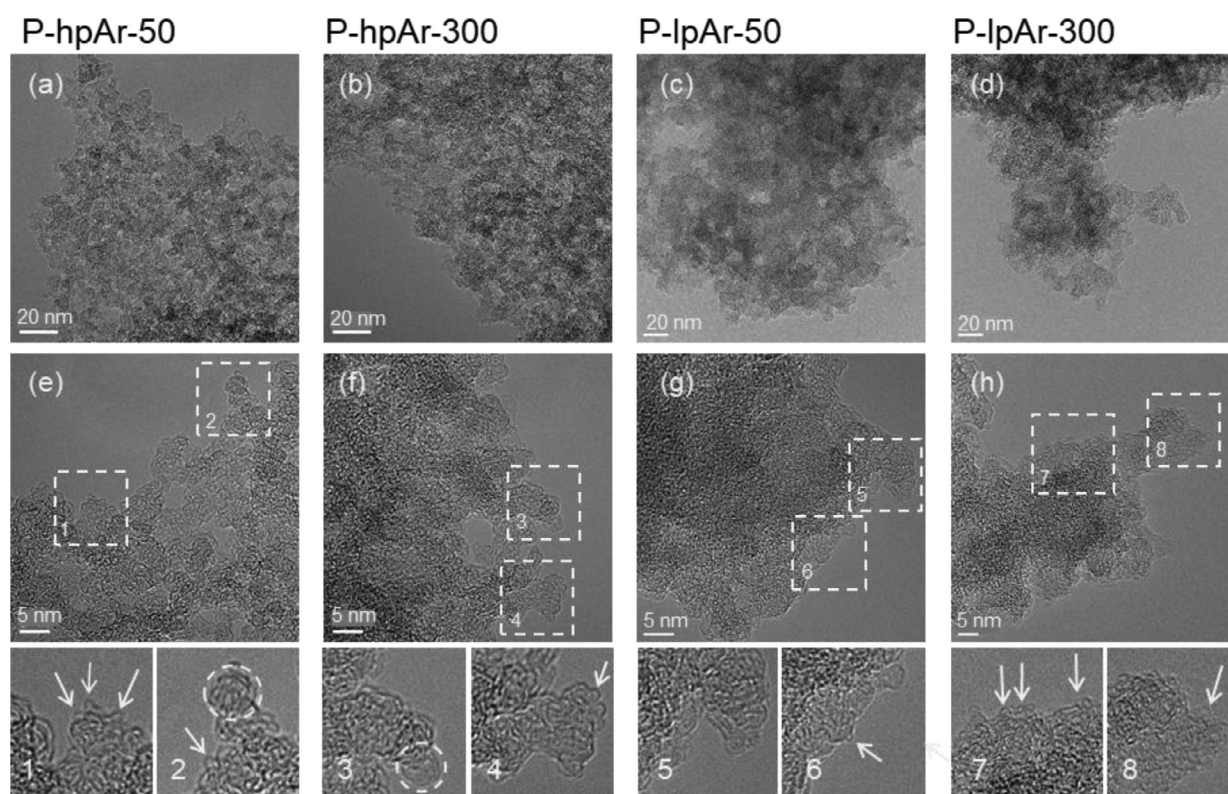
Fig. 6. TEM images of carbon nanoparticles produced with high and low purity Ar as dilution gas and two different spark frequencies. Nanostructural details in the areas marked with the dashed squares are shown enlarged in the images numbered 1 to 8.
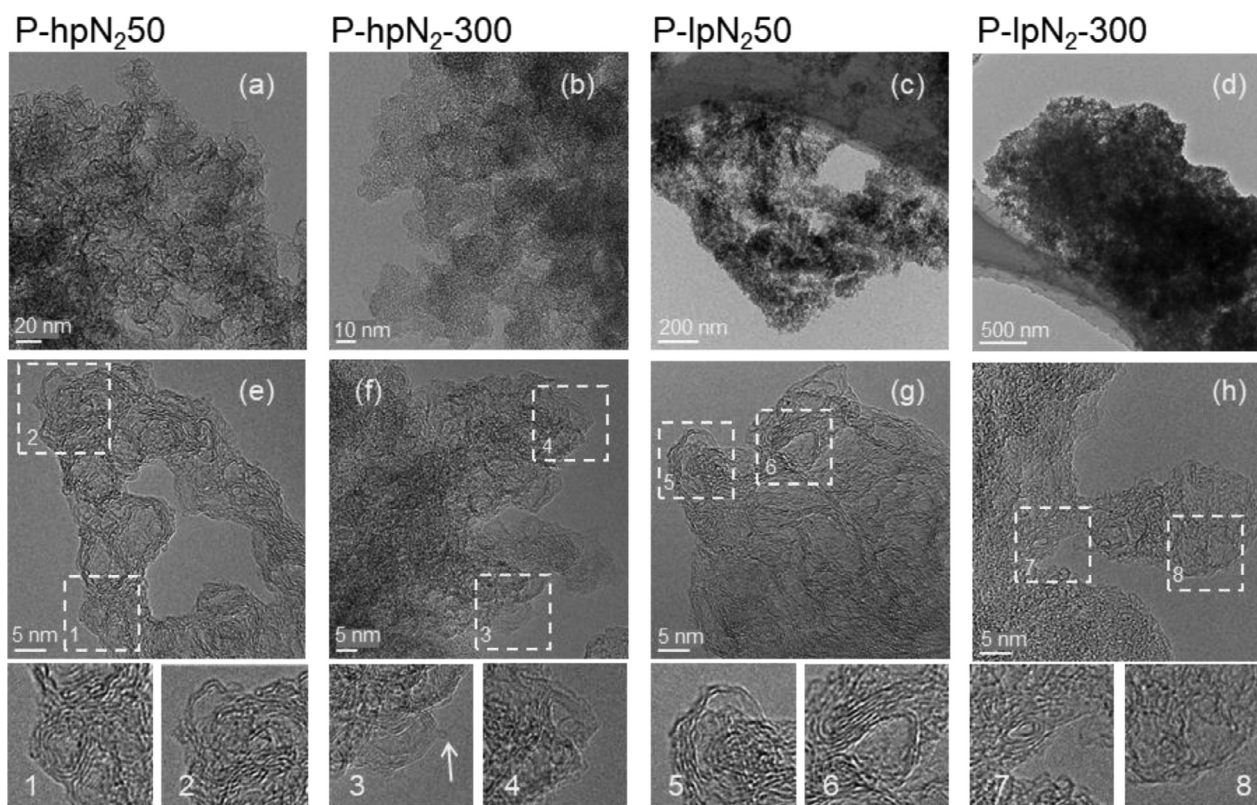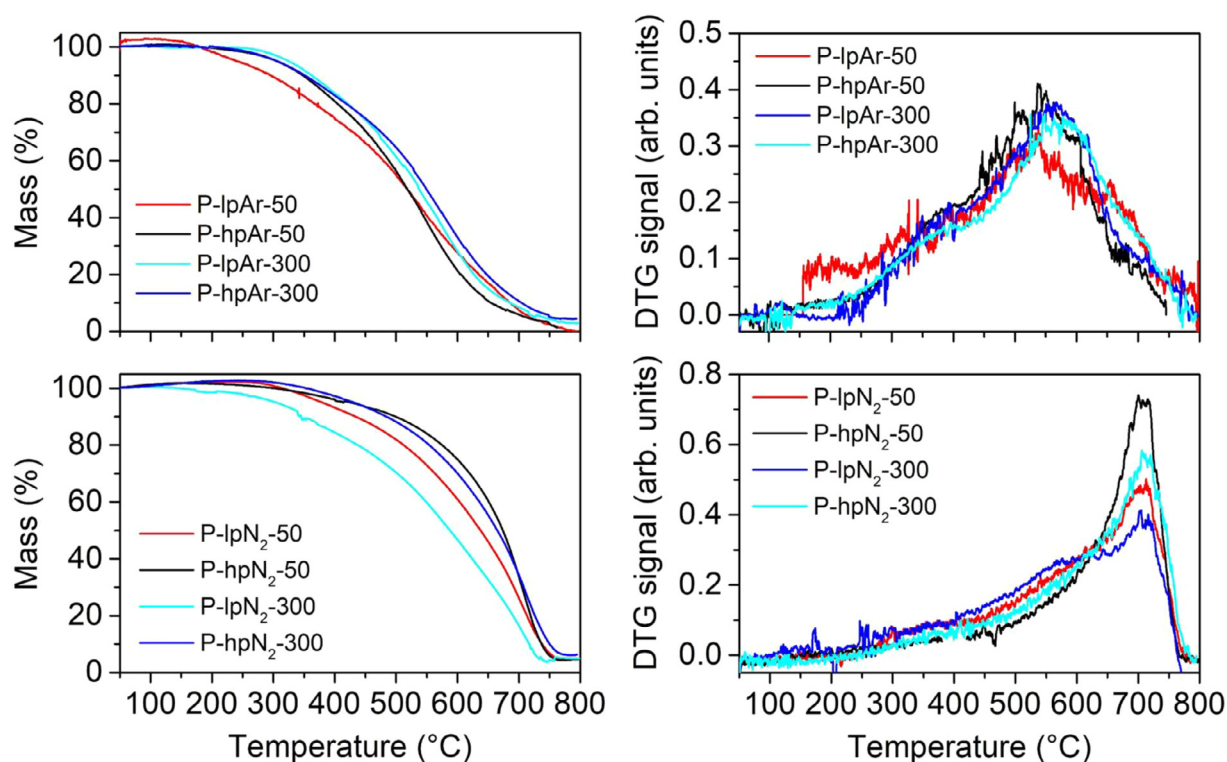

Fig. 7. TEM images of carbon nanoparticles produced with high and low purity N_2 as dilution gas and two different spark frequencies. Nanostructural details in the areas marked with the dashed squares are shown enlarged in the images numbered 1 to 8.

Fig. 8. Themogravimetric analysis results (left panels) and derivative curves (right panels) of carbon nanoparticles produced with high and low purity Ar (top panels) or with high and low purity N_2 (bottom panels) as dilution gas and two different spark frequencies.

acterized by only one important peak at 710 °C, a temperature higher than those corresponding to the two weight losses of particles produced with Ar; this points to a lower reactivity towards oxidation, as also stated by Hagen *et al.* in a recent work [22]. Surprisingly, in most cases between 100 and 350 °C a slight weight increase is detected; this highlights a propensity of the particles' surface functional groups towards oxygen addition during the heat treatment.

Looking at the TG curves in Fig. 8 (left panels), one concludes that the particles generated with a higher purity gas exhibit a lower reactivity towards oxygen since the main weight loss starts at a higher temperature. At the same gas purity, the high spark frequency allows for the production of particles more reactive towards oxidation, and this effect is more marked in the case of particles produced with a low purity dilution gas. Worthy of note in the shape of the DTG curve of P-lpN2-300 is also a shoulder peaked at 550 °C, indicative of the similarity between these particles and those produced in an Ar environment. The different oxidation behavior of particles produced with Ar and with N_2 is strictly associated with the different microstructures observed by HRTEM (Figs. 6,7). The strongly curved fulleroid structure of the primary particles produced with Ar can be easily functionalized with reactive groups, which are less stable than purely sp^2 hybridized carbon. The higher resistance against oxidation of the particles produced with N_2 is most likely due to the larger graphenic crystallites seen in the HRTEM micrographs (Fig. 7). As a general rule, large crystallites have a lower ratio of edge site to basal plane carbon atoms, thus a lower surface area prone to attack of the reactive groups [48].

4. Conclusions

The characteristics of carbonaceous nanoparticles produced by a Palas type SDG utilizing graphite rods were investigated to link the

SDG operative parameters to the composition, the chemical groups present and the morphology of the product. It was found that the nanotexture (and, as a consequence, the chemical reactivity and the surface chemistry) of the carbonaceous nanoparticles obtainable by a SDG system can be easily tuned by using different dilution gasses (nitrogen and argon) at different purity degree. The use of N_2 as dilution gas allowed for the incorporation of significant amounts of N (5–7 wt.%) in the carbonaceous particle network mainly as pyrrolic, graphitic N and N-oxide functional groups.

In all the investigated cases the nanostructure and arrangement of the particles noticeably differ in some aspects if compared to the soot typically emitted from combustion sources and internal combustion engines: 1) the average primary particle sizes are overall considerably smaller (from 2 to 5 nm in the case of particles produced with Ar as dilution gas and up to 10 nm in the case of particles produced with N_2 as dilution gas) and 2) the presence of N doping in the C network is scarcely present in soot emitted from real sources.

As a general consideration, the particles produced with N_2 as dilution gas at low purity could best mimic the airborne carbonaceous particulates since it well reproduces the smooth surfaces typical of the most real soot with more extended graphene sheets compared to the particles produced with Ar.

Overall, this study confirms the importance of carefully checking the operative SDG conditions due to their influence on the particles characteristics and this aspect becomes crucial when GfG generated nanoparticle aerosols serve as model soot in specific experiments.

Declaration of Competing Interest

The authors declare that they have no known competing financial interests or personal relationships that could have appeared to influence the work reported in this paper

CRediT authorship contribution statement

M. Alfè: Conceptualization, Investigation, Formal analysis, Writing – original draft, Writing – review & editing. **V. Gargiulo:** Investigation, Formal analysis, Validation, Writing – review & editing. **O. de Luca:** Investigation, Formal analysis, Validation, Writing – review & editing. **P. Rudolf:** Validation, Supervision, Writing – review & editing. **B. Zhang:** Investigation, Formal analysis. **P. Sabia:** Investigation, Formal analysis, Validation, Writing – review & editing. **M. De Joannon:** Conceptualization, Validation, Writing – review & editing, Supervision.

References

[1] D.E. Schraufnagel, The health effects of ultrafine particles, Exp. Mol. Med. 52 (2020) 311–317, doi:10.1038/s12276-020-0403-3.

[2] H. Sooryanarain, S. Elankumaran, Environmental role in influenza virus outbreaks, Annu. Rev. Anim. Biosci. 3 (2015) 347–373, doi:10.1146/annurev-animal-022114-111017.

[3] T.P. Weber, N.I. Stilianakis, Inactivation of influenza A viruses in the environment and modes of transmission: a critical review, J. Infect. 57 (5) (2008) 361–373, doi:10.1016/j.jinf.2008.08.013.

[4] B. Wang, J. Liu, Y. Li, S. Fu, X. Xu, L. Li, et al., Airborne particulate matter, population mobility and COVID-19: a multi-city study in China, BMC Public Health 20 (2020) 1585) article number, doi:10.1186/s12889-020-09669-3.

[5] L. Setti, F. Passarini, G. De Gennaro, P. Barbieri, M.G. Perrone, A. Piazzalunga, et al., The potential role of particulate matter in the spreading of COVID-19 in Northern Italy: first Evidence-based Research Hypotheses, medRxiv 2020.04.11.20061713, doi:10.1101/2020.04.11.20061713.

[6] M. Coccia, Factors determining the diffusion of COVID-19 and suggested strategy to prevent future accelerated viral infectivity similar to COVID, Sci. Total Environ. 729 (2020) 138474, doi:10.1016/j.scitotenv.2020.138474.

[7] M.F. Falcão Sobral, G.B. Duarte, G.P. Sobral, M.L. Monteiro Marinho, A. Souza Melo, Association between climate variables and global transmission of SARS-CoV-2, Sci. Total Environ. 729 (2020) 138997, doi:10.1016/j.scitotenv.2020.138997.

[8] E. Conticini, B. Frediani, D. Caro, D. Can atmospheric pollution be considered a co-factor in extremely high level of SARS-CoV-2 lethality in Northern Italy? Environ. Poll. 261 (2020) 114465, doi:10.1016/j.envpol.2020.114465.

[9] X. Wu, R.C. Nethery, M.B. Sabath, D. Braun, F. Dominici, (2020) Exposure to air pollution and COVID-19 mortality in the United States: a nationwide cross-sectional study. medRxiv 2020.04.05.20054502, doi:10.1101/2020.04.05.20054502.

[10] L. Peng, X. Zhao, Y. Tao, S. Mi, J. Huang, Q. Zhang, The effects of air pollution and meteorological factors on measles cases in Lanzhou, China, Environ. Sci. Pollut. Res. 27 (2020) (2020) 13524–13533, doi:10.1007/s11356-020-07903-4.

[11] L. Setti, F. Passarini, G. De Gennaro, P. Barbieri, M.G. Perrone, M. Borelli, et al., Airborne Transmission Route of COVID-19: why 2 Meters/6 Feet of Inter-Personal Distance Could Not Be Enough, Int. J. Environ. Res. Pub. Health 17 (2020) 2932, doi:10.3390/ijerph17082932.

[12] L. Setti, F. Passarini, G. De Gennaro, P. Barbieri, A. Pallavicini, M. Ruscio, et al., Searching for SARS-COV-2 on particulate matter: a possible early indicator of COVID-19 epidemic recurrence, Int. J. Environ. Res. Public Health 17 (2020) 2986, doi:10.3390/ijerph17092986.

[13] L. Setti, F. Passarini, G. De Gennaro, P. Barbieri, M.G. Perrone, A. Piazzalunga, Is There a Plausible Role for Particulate Matter in the spreading of COVID-19 in Northern Italy? BMJ 368 (2020) m1103, doi:10.1136/bmj.m1103.

[14] L. Setti, F. Passarini, G. De Gennaro, P. Barbieri, M.G. Perrone, M. Borelli, et al., SARS-Cov-2RNA found on particulate matter of Bergamo in Northern Italy: first evidence, Environ. Res. 188 (2020) 109754–109759, doi:10.1016/j.envres.2020.109754.

[15] L. Becchetti, G. Conzo, P. Conzo, F. Salustri, Understanding the Heterogeneity of Adverse COVID-19 outcomes: the role of poor quality of air and lockdown decisions, (2020) Available at SSRN: https://ssrn.com/abstract=3572548 or http://dx.doi.org/ 10.2139/ssrn.3572548;

[16] Y. Yao, J. Pan, W. Wang, Z. Liu, H. Kan, Y. Qiu, et al., Association of particulate matter pollution and case fatality rate of COVID-19 in 49 Chinese cities, Sci. Total Environ. 741 (2020) 140396–140401, doi:10.1016/j.scitotenv.2020.140396.

[17] Y. Su, M.F. Sipin, K.A. Prather, R.M. Gelein, A. Lunts, G. Oberdorster, ATOFMS characterization of individual model aerosol particles used for exposure studies, Aerosol Sci. Tech. 39 (2005) 400–407, doi:10.1080/027868290946694.

[18] B.O. Meuller, M.E. Messing, D.L.J. Engberg, A.M. Jansson, L.I.M. Johansson, S.M. Norlen, et al., Review of Spark Discharge Generators for Production of Nanoparticle Aerosols, Aerosol Sci. Tech. 46 (2012) 1256–1270, doi:10.1080/02786826.2012.705448.

[19] A. Sadezky, H. Muckenhuber, H. Grothe, R. Niessner, U. Poschl, Raman microspectroscopy of soot and related carbonaceous materials: spectral analysis and structural information, Carbon 43 (2005) 1731–1742, doi:10.1016/j.carbon.2005.02.018.

[20] C. Helsper, W. Molter, F. Loffler, C. Wadenpohl, S. Kaufmann, G. Wenninger, Investigations of a new aerosol generator for the production of carbon aggregate particles, Atmos. Environ., Part A 27 (8) (1993) 1271–1275, doi:10.1016/0960-1686(93)90254-V.

[21] N.S. Tabrizi, M. Ullmann, V.A. Vons, U. Lafont, A. Schmidt-Ott, Generation of nanoparticles by spark discharge, J. Nanopart. Res. 11 (2009) 315–332, doi:10.1007/s11051-008-9407-y.

[22] F.P. Hagen, A. Rinkenburger, J. Günther, H. Bockhorn, R. Niessner, R. Suntz, et al., Spark discharge-generated soot: varying nanostructure and reactivity against oxidation with molecular oxygen by synthesis conditions, J. Aerosol Sci. 143 (2020) 105530, doi:10.1016/j.jaerosci.2020.105530.

[23] M. de Joannon, M. Alfè, G. Cozzolino, V. Gargiulo, P. Sabia, R. Ragucci, Removal of very small submicrometric particles by water nucleation: effects of chemical−physical properties of particles, Energy Fuels 32 (2018) 10285–10294, doi:10.1021/acs.energyfuels.8b01142.

[24] C. Roth, G.A. Ferron, E. Karg, B. Lentner, G. Schumann, S. Takenaka, J. Heyder, Generation of ultrafine particles by spark discharging, Aerosol Sci. Technol. 38 (2004) 228–235, doi:10.1080/02786820490247632.

[25] O. Ivashenko, H. Logtenberg, J. Areephong, A.C. Coleman, P.V. Wesenhagen, E.M. Geertsema, N. Heureux, B.L. Feringa, P. Rudolf, W.R. Browne, Remarkable stability of high energy conformers in self-assembled monolayers of a bistable electro- and photoswitchable overcrowded alkene, J. Phys. Chem. C 115 (2011) 22965–22975 doi.org/10.1021/jp206889y.

[26] J.F. Moulder, W.F. Stickle, P.E. Sobol, Handbook of X-Ray Photoelectron Spectroscopy Perkin-Elmer, Physical Electronics Division, USA, 1993.

[27] D. Shirley, High-resolution X-ray photoemission spectrum of the valence bands of gold, Phys. Rev. B 5 (1972) 4709–4714, doi:10.1103/PhysRevB.5.4709.

[28] D.E. Evans, R.M. Harrison, J.G. Ayres, The generation and characterisation of elemental carbon aerosols for human challenge studies, J. Aerosol Sci. 34 (8) (2003) 1023–1041, doi:10.1016/S0021-8502(03)00069-7.

[29] K. Dimos, F. Arcudi, A. Kouloumpis, I.B. Koutselas, P. Rudolf, D. Gournis, et al., Top-down and bottom-up approaches to transparent, flexible and luminescent nitrogen-doped carbon nanodot-clay hybrid films, Nanoscale 9 (29) (2017) 10256–10262, doi:10.1039/C7NR02673K.

[30] A. Kouloumpis, E. Thomou, N. Chalmpes, K. Dimos, K. Spyrou, A.B. Bourlinos, et al., Graphene/carbon dot hybrid thin films prepared by a modified langmuir-schaefer method, ACS Omega 2 (5) (2017) 2090–2099, doi:10.1021/acsomega.7b00107.

[31] R. Wang, Y. Wang, C. Xu, J. Sun, L. Gao, Facile one-step hydrazine-assisted solvothermal synthesis of nitrogen-doped reduced graphene oxide: reduction effect and mechanisms, RSC Adv 3 (2013) 1194–1200, doi:10.1039/C2RA21825A.

[32] A. Ganguly, S. Sharma, P. Papakonstantinou, J. Hamilton, Probing the thermal deoxygenation of graphene oxide using high-resolution in situ X-ray-based spectroscopies, J. Phys. Chem. C 115 (34) (2011) 17009–17019, doi:10.1021/jp203741y.

[33] J. Russat, Characterization of polyamic acid/polyimide films in the nanometric thickness range from spin-deposited polyamic acid, Surf. Interface Anal. 11 (1988) 414–420, doi:10.1002/sia.740110803.

[34] H. Kiuchi, T. Kondo, M. Sakurai, D. Guo, J. Nakamura, H. Niwa, et al., Characterization of nitrogen species incorporated into graphite using low energy nitrogen ion sputtering, Phys Chem Chem Phys 18 (2016) 458–465, doi:10.1039/C5CP02305J.

[35] J.C. Moreno-López, F. Fedi, G. Argentero, M. Carini, J. Chimborazo, J. Meyer, et al., Exclusive substitutional nitrogen doping on graphene decoupled from an insulating substrate, J. Phys. Chem. C 124 (40) (2020) 22150–22157, doi:10.1021/acs.jpcc.0c06415.

[36] J. Pels, F. Kapteijn, J. Moulijn, Q. Zhu, K. Thomas, Evolution of nitrogen functionalities in carbonaceous materials during pyrolysis, Carbon N Y 33 (1995) 1641–1653, doi:10.1016/0008-6223(95)00154-6.

[37] U. Kirchner, V. Scheer, R. Vogt, FTIR spectroscopic investigation of the mechanism and kinetics of the heterogeneous reactions of NO2 and HNO3 with soot, J. Phys. Chem. A 104 (2000) 8908–8915, doi:10.1021/jp0005322.

[38] M. Kalberer, M. Ammann, F. Arens, H.W. Gaggeler, U. Baltensperger, Heterogeneous formation of nitrous acid (HONO) on soot aerosol particles, J. Geoph. Res. 104 (1999) 13825–13840, doi:10.1029/1999JD900141.

[39] B.O. Meuller, M.E. Messing, D.L.J. Engberg, A.M. Jansson, L.I.M. Johansson, S.M. Norlén, et al., Review of spark discharge generators for production of nanoparticle aerosols, Aerosol Sci. Technol. 46 (2012) 1256–1270, doi:10.1080/02786826.2012.705448.

[40] V. Țucureanu, A. Matei, M. Avram, FTIR spectroscopy for carbon family study, Crit. Rev. Anal. Chem. 46 (2016) 502–520, doi:10.1080/10408347.2016.1157013.

[41] A. Enotiadis, K. Angjeli, N. Baldino, I. Nicotera, D. Gournis, Graphene-based nafion nanocomposite membranes: enhanced proton transport and water retention by novel organo-functionalized graphene oxide nanosheets, Small 8 (2012) 3338–3349, doi:10.1002/smll.201200609.

[42] K. Tian, Z. Su, H. Wang, X. Tian, W. Huang, C. Xiao, N-doped reduced graphene oxide/waterborne polyurethane composites prepared by in situ chemical reduction of graphene oxide, Composites: Part A 94 (2017) 41–49, doi:10.1016/j.compositesa.2016.11.020.

[43] J. Przepiorski, Enhanced adsorption of phenol from water by ammonia-treated activated carbon, J. Hazard. Mater. B135 (2006) 453–456, doi:10.1016/j.jhazmat.2005.12.004.

[44] H. Ding, J.-.S. Wei, H.-.M. Xiong, Nitrogen and sulfur co-doped carbon dots with strong blue luminescence, Nanoscale 6 (2014) 13817.

[45] Y.V. Fedoseeva, E.V. Lobiak, E.V. Shlyakhova, K.A. Kovalenko, V.R. Kuznetsova, A.A. Vorfolomeeva, et al., Hydrothermal activation of porous nitrogen-doped carbon materials for electrochemical capacitors and sodium-ion batteries, Nanomaterials 10 (2020) 2163, doi:10.3390/nano10112163.

[46] A. Majumdar, S.C. Das, T. Shripathi, J. Heinicke, R. Hippler, Shake up satellites and fluorescence property of carbon nitride and hydrogenated carbon nitride: annealing effect, Surf Sci 609 (2013) 53–61, doi:10.1016/j.susc.2012.11.003.

[47] N. Mutsukura, K. Akita, Infrared absorption spectroscopy measurements of amorphous CN films prepared in CH_4/N_2 r.f. discharge, Thin Solid Films 349 (1999) 115–119, doi:10.1016/S0040-6090(99)00237-0.

[48] M. Alfè, B. Apicella, R. Barbella, J.-.N. Rouzaud, A. Tregrossi, A. Ciajolo, Structure-property relationship in nanostructures of young and mature soot in premixed flames, Proc. Combust. Inst. 32 (2009) 697–704, doi:10.1016/j.proci.2008.06.193.

[49] C. Russo, M. Alfè, J.-.N. Rouzaud, F. Stanzione, A. Tregrossi, A. Ciajolo, Probing structures of soot formed in premixed flames of methane, ethylene and benzene, Proc. Combust. Inst. 34 (1) (2013) 1885–1892, doi:10.1016/j.proci.2012.06.127.

[50] V. Gargiulo, M. Alfè, G. Di Blasio, C. Beatrice, Chemico-physical features of soot emitted from a dual-fuel ethanol–diesel system, Fuel 150 (2015) 154–161, doi:10.1016/j.fuel.2015.01.096.

[51] C. Guido, M. Alfè, V. Gargiulo, P. Napolitano, C. Beatrice, N. Del Giacomo, Chemical/physical features of particles emitted from a modern automotive dual-fuel methane–diesel engine, Energy Fuels 32 (10) (2018) 10154–10162, doi:10.1021/acs.energyfuels.8b01011.

[52] C. Arnal, M. Alfè, V. Gargiulo, A. Ciajolo, M.U. Alzueta, A. Millera, et al., Characterization of soot, in: F Battin-Leclerc, JM Simmie, E Blurock (Eds.), Developing Detailed Chemical Kinetic Models series: Green Energy and technology, London Limited, Springer-Verlag, 2013, pp. 333–362.

[53] J.-.O. Müller, D.S. Su, R.E. Jentoft, J. Kröhnert, F.C. Jentoft, R. Schlögl, Morphology-controlled reactivity of carbonaceous materials towards oxidation, Catal Today 102–103 (2005) 259–265, doi:10.1016/j.cattod.2005.02.025.

[54] L. Henrard, F. Malengreau, P. Rudolf, K. Hevesi, R. Caudano, Ph. Lambin, et al., Electron energy loss spectroscopy of plasmon excitations in concentric-shell fullerenes, Phys. Rev. B 59 (1999) 5832–5836, doi:10.1103/PhysRevB.59.5832.

Michela Alfè is a Researcher at the Institute of Science and Technology for Sustainable Energy and Mobility (CNR-STEMS), previously CNR-IRC located in Naples, Italy. She graduated in Chemistry and obtained a PhD in Chemical Engineering. Her highly inter- or multi-disciplinary activities are focused in two strategic areas: Energy and Environment and Material Science and include the synthesis of innovative materials for applications in energetic (solid sorbents for CCS, water treatment, sensoristic, photoactive materials, bioelectronics).

Valentina Gargiulo holds a Master's Degree (2005) and a PhD (2009) in Chemistry, from the University Federico II, Naples (Italy). In July 2020 she got a position as Researcher at Italian Research Council (CNR) and since October 2020 she is member of STEMS-CNR permanent staff. Her research activities deal with the synthesis and characterization of advanced materials, the characterization and treatment of pyrolysis feedstocks and products and the chemico-physical analysis of complex carbonaceous materials.


Dr. Oreste de Luca studied physics at the Università della Calabria, Arcavacata di Rende (Italy), and did part of his master project in the Department of Chemistry of the University of Warwick (U.K.) as ERASMUS student. He obtained his PhD with a project on "Self-assembled monolayers of organic molecules on noble metals and two-dimensional materials", also from the Università della Calabria. As PhD student he spent 5 months at the École Polytechnique Fédérale de Lausanne (Switzerland). In 2018 he joined the Zernike Institute for Advanced Materials in Groningen, NL as a postdoctoral fellow.

Professor Petra Rudolf studied physics at the Università La Sapienza in Rome (Italy) and then had an international career which took her from the TASC-INFM laboratory in Trieste, where she switched to Surface Science, to Bell Labs, NJ (USA), where she pioneered fullerene research, and then to the Facultés Universitaires Notre Dame de la Paix in Namur (Belgium) where she continued to work on carbon allotropes. Since 2003 she has the Chair in Experimental Solid State Physics at the University of Groningen where she also heads the Surfaces and Thin Films group of the Zernike Institute for Advanced Materials.

Bingsen Zhang obtained the Ph.D. degree at Northeastern University (China) in 2009, and then went to Fritz Haber Institute of Max Planck Society in Berlin (Germany) as a postdoctoral fellow in the Department of Inorganic Chemistry. In 2011, he joined Institute of Metal Research (IMR), Chinese Academy of Sciences (CAS) and received an IMR SYNL-T.S. Kê Research Fellowship founded by Shenyang National Laboratory for Materials Science (SYNL). Now he is a professor of IMR CAS. His main research interest is the microstructure investigation of nanocatalysts and energy conversion and storage materials.
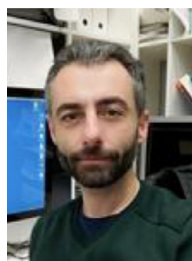
Pino Sabia is a Researcher at the Institute of Science and Technology for Sustainable Energy and Mobility (STEMS), previously IRC – CNR located in Naples, Italy. He graduated in Chemical Engineering, University of Naples Federico II, Naples, and he obtained a PhD in Chemical Engineering at the same department. His research interests focus on experimental study of non-conventional combustion processes (MILD/Oxy-fuel) in model reactors and lab-scale burners by means of chemical and optical diagnostic techniques. He is an expert on numerical simulations of complex chemical kinetics for the oxidation of traditional and new-generation fuels, formation and abatement of pollutants.

Mara de Joannon is senior researcher at the Institute of Science and Technology for Sustainable Energy and Mobility of the Italian National Research Council (CNR) in Napoli (Italy). She obtained her master's and Ph.D. degrees at University Federico II in Napoli. She is a Fellow of The Combustion Institute (CI) and member of CI Board of Directors (2020–2026), Associated Editor of Proceedings of the Combustion Institute and Editorial Board Member of Combustion and Flame. Her main scientific interests are smart energy carriers, advanced/fuel-flexible combustion processes as MILD/flameless/diluted combustion, pollutant formation and abatement.